Research Square

Preprints are preliminary reports that have not undergone peer review.
They should not be considered conclusive, used to inform clinical practice,
or referenced by the media as validated information.

A hybrid biorthogonal wavelet and superimposed current scheme for fast fault detection and classification on a 400 kV, 400 km transmission line

Abhay Yadav
Sharda University
Soma Deb
soma.deb@sharda.ac.in

Sharda University

Research Article

Keywords: Transmission line protection, Fault detection, Fault classification, bior5.5 wavelet, Superimposed currents, Travelling waves

Posted Date: November 18th, 2026

DOI: https://doi.org/10.21203/rs.3.rs-11398011/v1

License: This work is licensed under a Creative Commons Attribution 4.0 International License.
Read Full License

Additional Declarations: No competing interests reported.

A hybrid biorthogonal wavelet and superimposed current scheme for fast fault detection and classification on a 400 kV, 400 km transmission line

Abhay Yadav[1] and Soma Deb[1*]

[1*]Department of Electrical, Electronics and Communication Engineering, Sharda University, Greater Noida, Uttar Pradesh, India.

*Corresponding author(s). E-mail(s): soma.deb@sharda.ac.in;
Contributing authors: 2024102693.abhay@dr.sharda.ac.in;

Abstract

Long extra-high-voltage lines need protection that detects and types a fault within milliseconds. This paper proposes a two-stage relaying principle for a 400 kV, 50 Hz, 400 km transmission line. A level 1 biorthogonal (bior5.5) wavelet transform of relay currents captures the 5–10 kHz fault transient and raises the trip flag, after which half cycle RMS values of the superimposed phase and residual currents identify the faulted phases and any earth involvement. A MATLAB/Simulink model produced 462 fault records, covering eleven fault types, seven distances from 50 to 350 km and six fault resistances from 10 to 60 **Ω**, plus one healthy record. Thresholds were fitted on part of the data and tested on unseen resistances or distances. Every fault was detected without a spurious trip, with mean delays of 0.27–1.50 ms that follow the wave travel time. All withheld faults were typed correctly when the identical ABC and ABCG faults form one class (90.9–91.0% with eleven classes). The ground mode was found to dominate the high frequency transient of earth faults, which limits phase selection by the wavelet alone. The superimposed current stage stayed fully accurate down to 20 dB SNR, whereas the wavelet trigger needed about 60 dB.

Keywords: Transmission line protection, Fault detection, Fault classification, bior5.5 wavelet, Superimposed currents, Travelling waves

1 Introduction

Bulk power in modern grids is moved over long extra-high-voltage (EHV) corridors, and these overhead lines are the components most often hit by lightning, insulation breakdown, vegetation contact and storms. Once a short circuit appears on such a corridor, the relay has a budget of only a few milliseconds to sense it, pick out the phases involved and decide whether earth is part of the fault path. That information drives which breaker poles open, whether single-pole autoreclosing may be attempted and, ultimately, whether neighbouring generators remain in synchronism[1, 2]. Shortening this chain by even one millisecond lowers the thermal and mechanical stress on equipment and widens the transient-stability margin.

A 400 km line makes this task harder in three ways. The current seen at the relaying point shrinks markedly as the fault moves towards the far end and as the fault resistance grows. Any transient produced at the fault point needs more than a millisecond to travel back to the relay when the fault is distant. Finally, one set of measured currents has to support both the trip decision and the identification of eleven distinct fault [3–5]. Relays that work with fundamental frequency phasors, such as distance, overcurrent and current-differential elements, must wait roughly one power cycle for a stable phasor estimate, and their reach is affected by fault resistance, power swings and line arrangement[6–8].

Schemes that act on the fault-generated transient avoid this wait of one cycle. The high frequency burst created at the instant of breakdown rides on the first travelling wave and already encodes when, where and how the fault occurred[9, 10]. The discrete wavelet transform (DWT) is now the dominant way of extracting such bursts: a multiresolution filter bank splits a signal into octave bands while keeping precise timing, and its cost per sample is small[11–13]. Biorthogonal wavelets are attractive in this role because their analysis and synthesis filters are compactly supported and symmetric, which gives linear phase[14]. A recent investigation of a 300 km, 400 kV line reported that level-1 bior5.5 coefficients distinguish faulted phases from sound ones[1].

Moving such a scheme to a longer line raises several questions that decide whether it can be trusted in service. How do the level-1 coefficients change with distance to the fault and with fault resistance? Are their magnitudes, on their own, enough to name the faulted phases for every fault type? How close does the detection delay come to the physical limit set by wave propagation? And does the scheme stay secure when the current measurements contain noise? The present work answers these questions through a systematic simulation study of a 400 kV, 50 Hz, 400 km line, and turns the answers into a fast and noise tolerant hybrid relaying principle.

The principle uses two complementary views of the same currents. Level-1 bior5.5 detail coefficients in the 5–10 kHz band flag the disturbance within a fraction of a millisecond. The superimposed (delta) phase and residual currents over the next half cycle then identify the faulted phases and any earth involvement. Every threshold is learned from simulated training cases and checked on fault resistances and fault locations that were excluded from training.

This work makes five contributions:

- **Verified fault database.** A 400 kV line model built from eight 50 km sections produced 462 fault records (eleven fault types, seven distances from 50 to 350 km and six resistances from 10 to 60 Ω) plus one healthy record, each screened by automated physical consistency tests.
- **Insight into the level-1 transient.** The dependence of the bior5.5 D1 coefficients on fault type, distance, resistance and inception angle is quantified; the mother wavelet and the decomposition level are chosen from 15 candidates and six levels; and the 5–10 kHz content of earth faults is shown to be governed by the ground propagation mode.
- **Fast two-stage relaying principle.** Detection with D1, whose mean delay of 0.27–1.50 ms follows the wave travel time, is paired with half cycle superimposed current phase and earth identification, so that the fault type is available no later than 11.75 ms after inception.
- **Strict testing on unseen cases.** Thresholds are fitted on one group of operating conditions and assessed on unseen resistances and unseen distances; all withheld faults are assigned correctly when the electrically indistinguishable ABC and ABCG faults are counted as one three-phase class.
- **Noise behaviour and low computational load.** The superimposed current stage stays fully correct, without false trips, down to an SNR of 20 dB, whereas the wavelet trigger needs an SNR above about 60 dB; the whole scheme requires a single filtering stage and a handful of arithmetic operations per sample, which fits numerical relay hardware.

Section 2 surveys earlier work on wavelet-based, travelling-wave and fault-component, and intelligent relaying and identifies open issues. Section 3 introduces the test network, the simulation model and the fault cases. Section 4 explains the methodology, covering the wavelet stage, the detection rule, the superimposed current classifier, threshold fitting and the test protocol. Section 5 presents and discusses the findings, and Section 6 summarises the work. Three appendices complete the paper: Appendix A walks through the computation for sample faults, Appendix B tabulates the outcome for every simulated fault, and Appendix C breaks down the response time.

2 Literature review

2.1 Wavelet transforms in line protection

Wavelets entered transmissionline protection in the late 1990s, initially to locate faults from travelling-wave arrival times[15], and were soon extended to recognising and typing faults. Silva and colleagues fed wavelet-derived features to a neural network[16]; He and colleagues measured the singular entropy of wavelet coefficients on EHV circuits[17]; and Costa tracked the coefficient energy in real time to flag fault-induced transients[18]. The same tool has been adapted to lines with series capacitors[19], to schemes that detect, type and locate faults together[20], to very fast DWT and neural network detectors[21] and, through the stationary wavelet transform combined with support vector regression, to fault location[22].

A second group of studies examined the design choices behind wavelet-based relaying. Adly and colleagues discussed the pitfalls of wavelet-based fault identification on HV circuits[23]; Ananthan and colleagues used multiresolution analysis for online fault analysis[24]; and Borghetti and colleagues combined several time and frequency decompositions to locate faults in distribution feeders and confirmed the method experimentally[25]. Shalby and colleagues compared mother wavelets and decomposition depths for distribution feeders in a systematic way[26]. Other applications include locating lightning strokes[27], protecting feeders against shunt and high-impedance faults[28], intelligent circuit breaker releases[29] and wavelet-enhanced overcurrent relays[30]. Level-1 bior5.5 coefficients compared against fixed thresholds were recently used on a 300 km, 400 kV circuit[1].

2.2 Travelling waves and fault components

Approaches built on travelling waves or on superimposed (fault) components discard the load contribution and respond only to the change caused by the fault. Dong and colleagues identified the fault type and the faulted phases from the first current wave reaching the relay[10], and travelling-wave principles operating in microseconds have been proposed for VSC-based DC grids[31]. Chatterjee and Debnath built a line protection on positive-sequence fault components[32]; high frequency fault components form the basis of a distance element for large renewable plants[9]; and modal currents have been used to protect double-circuit lines[7]. Further indices, for example ones derived from the power spectral density[33] and versatile relaying algorithms[34], have been suggested for detecting and typing faults.

2.3 Learning-based methods

Data-driven classifiers are now common in fault typing, ranging from decision trees built on statistical descriptors[35] and support vector machines (SVMs)[36] to frameworks that extract features once and use them for both typing and locating[37]. Deep networks, including convolutional, long short-term memory (LSTM) and fully connected architectures, have been trained to detect, type and locate faults on transmission and distribution networks[38–41], and scalograms produced by wavelets have served as image inputs to convolutional networks using measurements from one line end[42]. Combinations of signal processing and learning have also been reported for high-resistance faults on DC microgrids[43] and, with wide-area measurements, for locating faults on compensated lines[44]. Broad surveys of these developments are available[2–4]. Table 1 groups representative studies according to the signal tool they use, the way they reach a decision and their purpose.

2.4 Open issues

Four open issues emerge from this survey and motivate the present study:

- Thresholds of wavelet-based schemes are frequently set and judged on one and the same set of simulations, so performance on unseen fault resistances or distances is seldom measured.

Table 1 Representative earlier studies grouped by signal processing tool, decision stage and purpose (as stated in the cited works).

Ref.	Signal tool / features	Decision method	Purpose
[16]	Wavelet coefficients	Neural network	Fault recognition and typing
[17]	Singular entropy of wavelet coefficients	Entropy criteria	Recognition and typing on EHV lines
[18]	Online coefficient energy	Fixed threshold	Transient recognition
[21]	Discrete wavelet transform	Neural network	High-speed recognition
[10]	First current travelling wave	Wave-based rules	Typing and phase selection
[32]	Positive-sequence fault components	Relay logic	Line protection
[33]	Power spectral density index	Index limits	Recognition and typing
[35]	Statistical descriptors	Decision tree	Typing
[38]	Automatically learned features	Deep network	Recognition and typing
[39]	Raw time series	LSTM network	Recognition, diagnosis, location
[42]	Wavelet scalogram images	Convolutional network	Typing from one line end
[26]	Choice of wavelet and level	Thresholds	Recognition on distribution feeders

- How the level-1 transient divides between propagation modes (especially how much of each phase current is ground mode) and what that means for phase identification has received little attention.
- Reported detection delays are rarely compared with the wave travel time, even though this travel time is the physical floor for any transient-based detector.
- Claims of noise immunity are usually not backed by a sweep over signal-to-noise ratios, although the highest wavelet band is the one most affected by broadband noise.

3 Test system and simulation framework

3.1 Network and line model

The investigated network is a two-source 400 kV, 50 Hz system in which a 400 km line connects bus S (sending end) to bus R (receiving end), as drawn in Fig. 1. Source G1 behind bus S has a 7 GVA short-circuit capacity and source G2 behind bus R a 10 GVA capacity, both with an X/R ratio of 10; G2 is 10° behind G1, which fixes the prefault power flow. Earthed-star loads of 50 MW, 24.2 Mvar and 500 MW, 213 Mvar are connected at buses S and R. The relay sits at bus S, where ideal sensors measure the three line currents and the residual current is formed in software. Table 2 collects all network data.

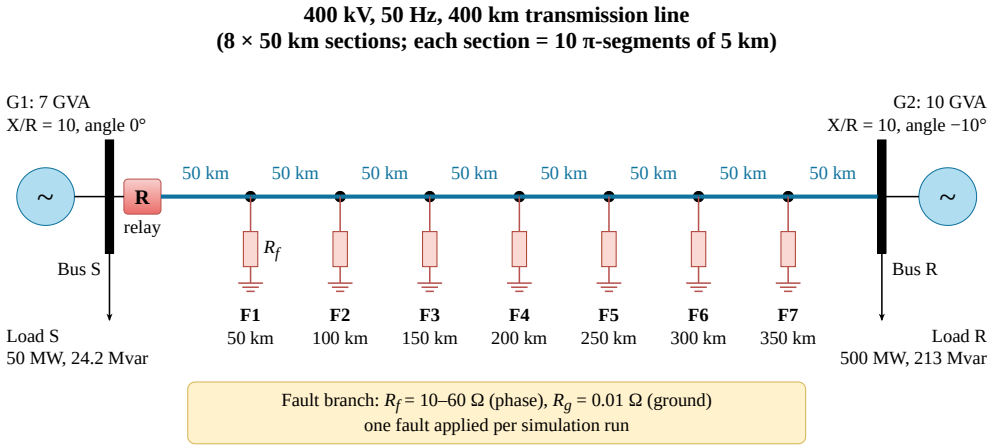


Fig. 1 One-line diagram of the simulated 400 kV network: relay at bus S and fault positions F1–F7 spaced 50 km apart along the 400 km line

The network was modelled in MATLAB/Simulink R2026a using Simscape Electrical, and Fig. 2 gives its block diagram. The line consists of eight 50 km sections, with a three-phase fault element attached to each of the seven intermediate buses (50–350 km). Each section is a cascade of ten 5 km π-segments carrying the positive- and zero-sequence data of Table 2, so that the positive-sequence wave speed is $1/\sqrt{L_1 C_1} = 2.90 \times 10^5$ km/s. For every run, a fault controller enables a single fault element with the chosen type, resistance and inception instant. The circuit equations are integrated with the fixed step trapezoidal rule[45] using a 50 μs step, identical to the 20 kHz relay sampling interval, after a 1 s healthy startup that brings every run to the same steady state.

3.2 Fault cases

All combinations of fault type, distance and fault resistance were simulated (Table 3). R_f is placed in series with each faulted phase and R_g in the earth return. Each run begins at the common healthy operating point and covers 0.2 s; the fault is switched in at t = 0.105 s, i.e. when the phase A voltage passes 90°, after five healthy cycles. Adding one healthy run yields 463 records of the three relay currents.

3.3 Consistency checks on the simulated data

Every one of the 463 records passed an automatic physical screening before signal processing began. The screening confirmed a logged step of exactly 50 μs; balanced (352 A rms per phase) and stationary prefault currents, with two successive cycles differing by under 0.01 %; a residual current of zero for every fault without earth and of at least 5 % of the phase current for every single- and double-phase-to-earth fault; a rise of more than 1.2 times in every faulted phase current; and a monotonic fall of the faulted phase current of single-phase-to-earth faults as R_f increases. None of these tests failed. One warning was raised for 170 records in which the raw samples

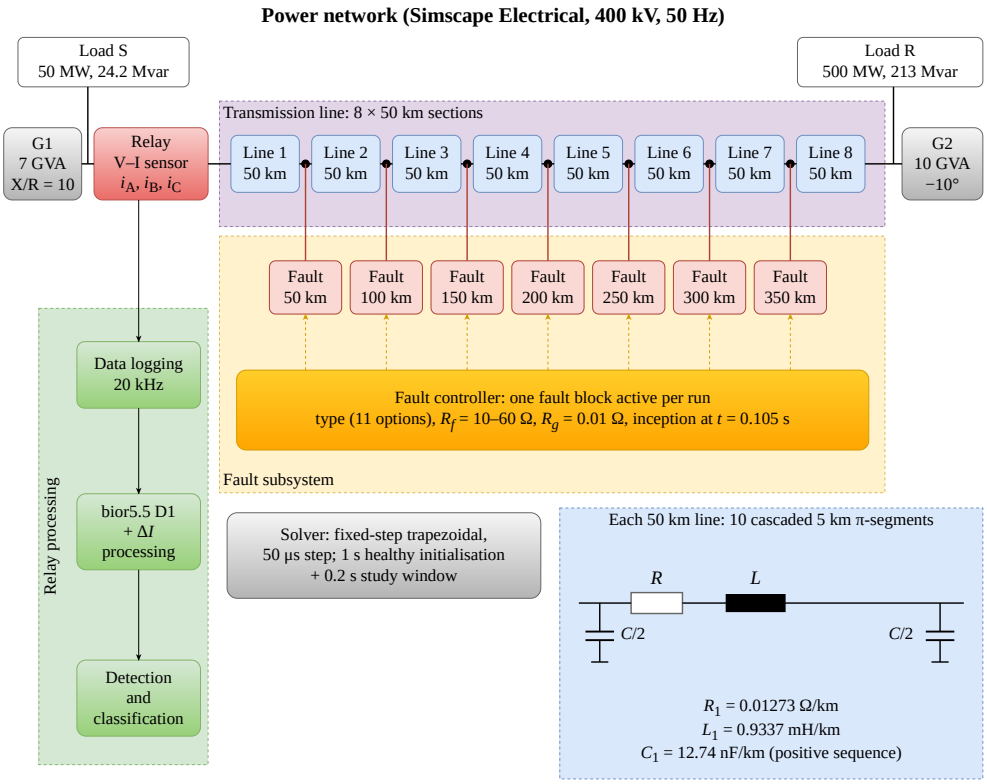


Fig. 2 Block diagram of the MATLAB/Simulink model: sources, relay sensor, eight 50 km line sections made of π-segments, seven fault elements commanded by the fault controller, and the processing chain

first changed more than 1 ms after the fault instant. These are the faults at 300–350 km, whose wavefront needs 1.0–1.2 ms to reach the relay; the BC faults, switched in at the zero crossing of the B–C voltage; and eight weak earth faults at 250 km.

4 Proposed methodology

4.1 Overview

Fig. 3 arranges the method in five stages. Stage 1 produces the relay currents with the simulation model. In stage 2, every current passes through a level-1 bior5.5 DWT while, in parallel, its superimposed component is formed. Stage 3 uses the detail coefficients to raise the fault flag, and stage 4 uses the superimposed currents of the subsequent half cycle to name the faulted phases and check for earth involvement. Stage 5 fits all thresholds on training cases and scores them on unseen cases, both with clean and with noisy signals.

Table 2 Electrical data of the simulated 400 kV network.

Quantity	Setting
Rated voltage; frequency	400 kV; 50 Hz
Source G1 at bus S	Short-circuit capacity 7 GVA, X/R 10, phase angle 0°
Source G2 at bus R	Short-circuit capacity 10 GVA, X/R 10, phase angle -10°
Line length and sections	400 km in 8 sections of 50 km; 10 π-segments (5 km) per section
Series resistance R_1 / R_0	0.01273 / 0.3864 Ω per km
Series inductance L_1 / L_0	0.9337 / 4.1264 mH per km
Shunt capacitance C_1 / C_0	12.74 / 7.751 nF per km
Positive-sequence wave speed	2.90 $\times 10^5$ km/s
Load at bus S	50 MW and 24.2 Mvar (0.90 lagging)
Load at bus R	500 MW and 213 Mvar (0.92 lagging)
Prefault current at the relay	352 A rms in each phase, balanced
Sampling rate; integration step	20 kHz; 50 μs fixed step trapezoidal
Resistance to earth R_g	0.01 Ω
Record length; fault instant	0.2 s; 0.105 s (v_A at 90°)

Table 3 Fault cases covered by the simulations.

Factor	Levels	Count
Fault type	AG, BG, CG, ABG, BCG, CAG, AB, BC, CA, ABC, ABCG	11
Distance from bus S	50, 100, 150, 200, 250, 300, 350 km	7
Fault resistance R_f	10, 20, 30, 40, 50, 60 Ω	6
Inception angle	v_A at 90° (t = 0.105 s)	1
Fault records	$11 \times 7 \times 6$	462
Healthy record	—	1
All records		**463**

4.2 Level-1 discrete wavelet transform with bior5.5

In the DWT, a sampled signal x[n] passes through a pair of analysis filters and each output is decimated by two[11]. Denoting the high-pass and low-pass analysis filters of length L by h_1 and h_0, the first level detail d_1 and approximation a_1 are

$$d_1[k] = \sum_{n=0}^{L-1} h_1[n]\, x[2k+1-n] \tag{1}$$

$$a_1[k] = \sum_{n=0}^{L-1} h_0[n]\, x[2k+1-n] \tag{2}$$

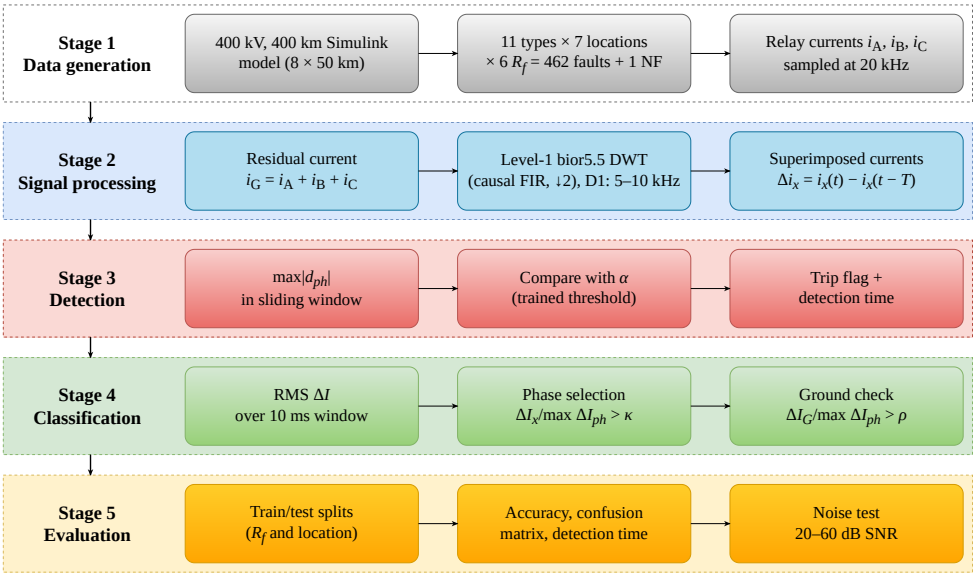


Fig. 3 The five stages of the proposed fault recognition and typing framework

Written as in Eq. (1), each detail coefficient uses only the present and earlier samples, which is the causal form a relay can evaluate. Decomposing the approximation again produces further detail levels D_j whose frequency ranges, for a sampling rate f_s, are

$$f_{D_j} \in \left[\frac{f_s}{2^{j+1}}, \frac{f_s}{2^j} \right] \tag{3}$$

With $f_s = 20$ kHz, D1 spans 5–10 kHz and D2 2.5–5 kHz, continuing down to D6 (156–312 Hz) and the approximation A6 (0–156 Hz). The bior5.5 wavelet comes from the biorthogonal spline family[14]; its symmetric high-pass analysis filter has linear phase and therefore a fixed group delay. The eleven nonzero coefficients of that filter are taken from the MATLAB Wavelet Toolbox. Fig. 4 depicts the single filtering stage executed in the relay.

4.3 Detection rule

Besides the three phase currents, the relay forms the residual current

$$i_G(n) = i_A(n) + i_B(n) + i_C(n) \tag{4}$$

The fault flag is raised as soon as the largest magnitude among the D1 coefficients of the three phases rises above the threshold α:

$$D = \max_{x \in \{A,B,C\}} \max_{k \in W_d} |d_{1,x}[k]|, \qquad \text{fault if } D > \alpha \tag{5}$$

Here W_d denotes a 5 ms moving window, and the detection time is measured from the fault instant to the first coefficient above α.

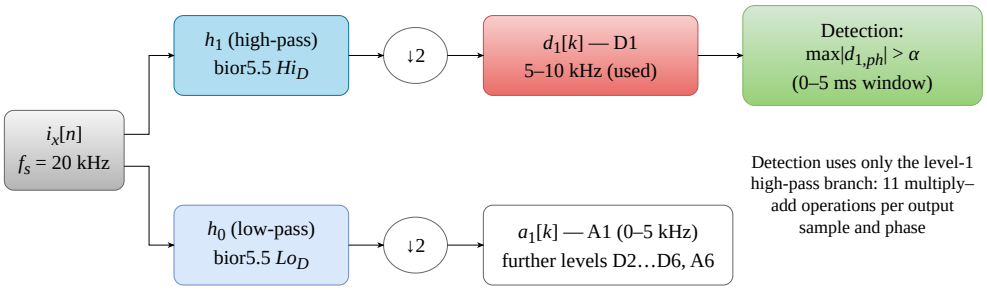


Fig. 4 Single filtering stage used for detection: only the high-pass path (D1, 5–10 kHz) is computed in the relay

4.4 Classification from superimposed currents

After the flag is raised, the faulted phases and earth involvement are obtained from superimposed currents, which strip away the load component by subtracting the value recorded one cycle before:

$$\Delta i_x(n) = i_x(n) - i_x(n-N), \qquad x \in \{A, B, C, G\} \tag{6}$$

with N $= f_s/f_0 = 400$ samples per cycle. Their RMS values over a half cycle window W_c containing M $= 200$ samples (10 ms) are

$$\Delta I_x = \sqrt{\frac{1}{M}\sum_{n \in W_c} \Delta i_x^2(n)} \tag{7}$$

In this study W_c starts at the fault instant; in a relay it would start at the detection instant, which is at most 1.75 ms later. Phase x ∈ A, B, C is marked as faulted when its normalised superimposed current is larger than κ, and earth involvement is marked when the normalised residual superimposed current is larger than ρ:

$$r_x = \frac{\Delta I_x}{\max(\Delta I_A, \Delta I_B, \Delta I_C)}, \qquad \text{phase } x \text{ faulted if } r_x > \kappa \tag{8}$$

$$g = \frac{\Delta I_G}{\max(\Delta I_A, \Delta I_B, \Delta I_C)}, \qquad \text{earth involved if } g > \rho \tag{9}$$

Fig. 5 gives the decision sequence. Three marked phases denote a three-phase fault and a single marked phase a phase-to-earth (L-G) fault; with two marked phases, the fault is phase-to-phase-to-earth (L-L-G) if g ¿ ρ and phase-to-phase (L-L) otherwise. A symmetrical three-phase fault carries no zero-sequence current, so ABC and ABCG faults produce identical currents and are reported together as one three-phase class.

4.5 Fitting the thresholds

α, κ and ρ are fitted to training data. If a threshold θ has to separate a set S^- of values that must stay below it (for instance, healthy windows in the case of α) from a set S^+ that must exceed it (fault windows), θ is placed at the geometric mean of the

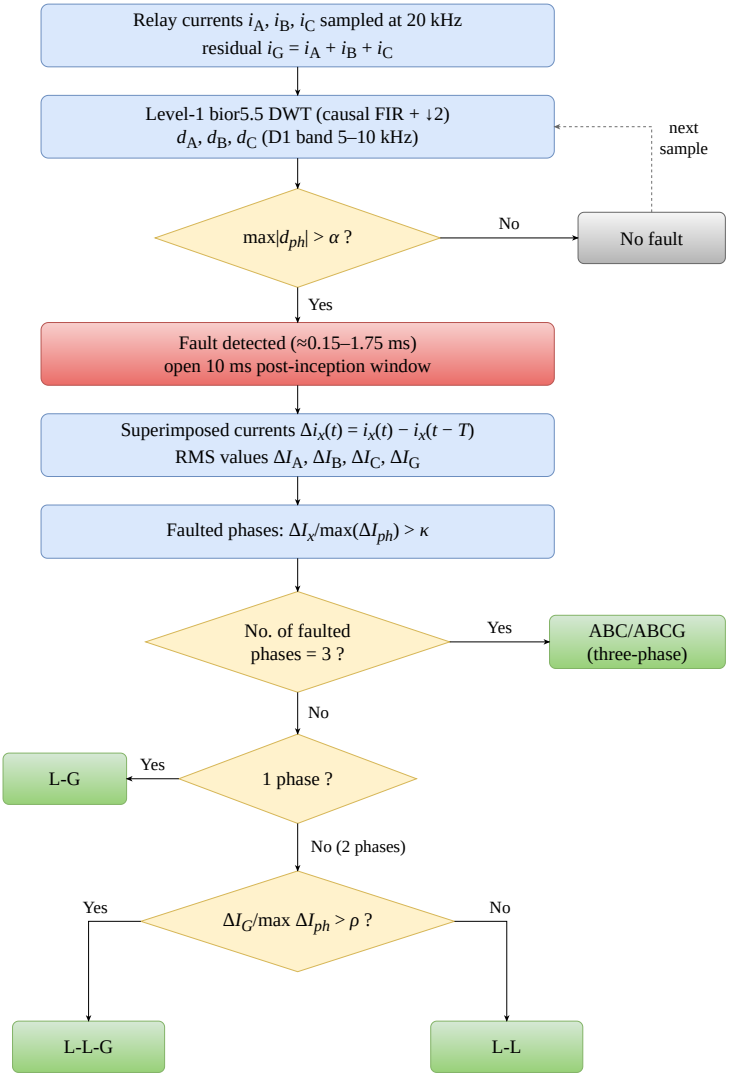


Fig. 5 Decision sequence of the proposed two-stage detection and typing scheme

two nearest members of the sets, and the separation margin μ is stored (when every member of S^- is zero, as for ρ, $\max(S^-)$ is replaced by $10^{-3}\cdot\min(S^+)$):

$$\theta = \sqrt{\max(S^-) \cdot \min(S^+)} \tag{10}$$

$$\mu = \frac{\min(S^+)}{\max(S^-)} \tag{11}$$

μ ¿ 1 indicates that the two training sets do not overlap and that the same relative headroom exists on either side of θ. The set S^- contains, for α, the prefault cycle of

every training record together with the healthy record; for κ, the normalised superimposed currents of sound phases; and for ρ, the normalised residual superimposed currents of faults without earth.

4.6 Learning-based classifiers on D1 features

To measure how much typing information the level-1 coefficients hold by themselves, two learning-based classifiers were trained on fourteen D1 features that do not depend on scale. These are the maxima of d_A, d_B, d_C and d_G, of the aerial mode details $d_x - d_G/3$ and of the phase difference details $d_A - d_B$, $d_B - d_C$ and $d_C - d_A$, each scaled by the largest phase maximum, together with the D1 energy fractions of the four signals. A random forest of 500 trees[46] and an SVM with a radial basis function kernel[47] were used; the SVM inputs were standardised.

4.7 Test protocol and noise model

No fault case was ever scored with a threshold or model fitted on that case; only the single healthy record serves as a healthy reference in both sets. Two splits were applied. In the R_f split, cases with $R_f = 10$, 30 and 50 Ω were used for fitting and those with 20, 40 and 60 Ω for testing (231 test faults). In the location split, faults at 50, 150, 250 and 350 km were used for fitting and those at 100, 200 and 300 km for testing (198 test faults). The healthy record and the prefault cycle of each record act as healthy windows. Typing accuracy is defined as

$$\mathrm{Acc} = \frac{N_{\mathrm{correct}}}{N_{\mathrm{test}}} \times 100\,\% \tag{12}$$

Robustness was examined by adding white Gaussian noise to every phase current, with a standard deviation fixed by the RMS current of the record and the chosen signal-to-noise ratio (SNR):

$$\sigma_x = \frac{\mathrm{RMS}(i_x)}{10^{\mathrm{SNR}/20}} \tag{13}$$

At each SNR (60, 50, 40, 30 and 20 dB), all thresholds and models were refitted on the noisy training records and scored on the noisy test records. The delay of the first wave from a fault at distance ℓ to the relay is

$$\tau = \frac{\ell}{v}, \qquad v = \frac{1}{\sqrt{L_1 C_1}} \tag{14}$$

5 Results and discussion

5.1 Fault current signatures and the level-1 response

Relay currents and D1 coefficients for four typical faults located 200 km from the relay with $R_f = 10$ Ω are plotted in Fig. 6. When the fault strikes, the currents of the faulted phases climb from 0.5 kA to peaks of 2–5.5 kA, while the D1 coefficients leap from under 0.41 A in the healthy state to 10–30 A. The D1 activity begins roughly

0.7 ms after inception, which is the time the first wavefront needs to cover 200 km, and it persists for several cycles.

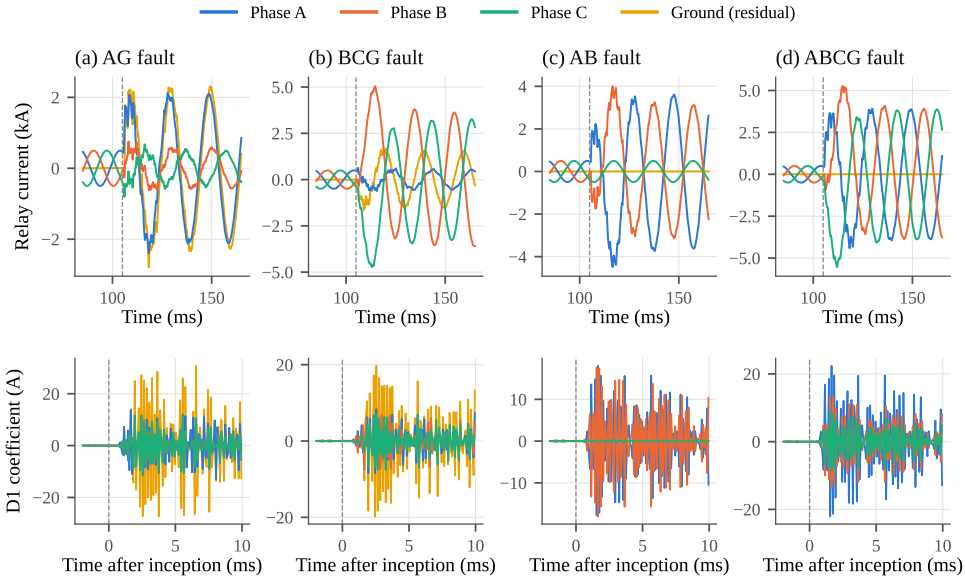


Fig. 6 Upper row: relay currents; lower row: level-1 bior5.5 detail coefficients during the first 10 ms, for (a) AG, (b) BCG, (c) AB and (d) ABCG faults 200 km from the relay with $R_f = 10\ \Omega$. Dashed lines mark the inception instant

The matching superimposed currents in Fig. 7 separate the fault contribution from the 352 A load current. Within the 10 ms classification window, the superimposed currents of the faulted phases reach peaks of 2.1–5.5 kA, while those of the healthy phases stay at or below 0.4 kA, and the residual superimposed current is large only when ground is involved.

Three features of these waveforms shape the classifier design. To begin with, the ground mode dominates the level-1 transient of earth faults: in the AG fault, the healthy phases B and C carry D1 bursts of 11.6 and 11.8 A, close to the 13.8 A of the faulted phase A, while the residual coefficient d_G reaches 28.5 A. Next, because v_A is at 90° at inception, the B–C voltage crosses zero at that moment; the phase-to-phase part of a BCG fault therefore launches hardly any transient and its D1 pattern resembles that of an L-G fault (Fig. 6b). Lastly, a symmetrical fault keeps the fault neutral at zero potential, so ABC and ABCG faults yield identical currents and $d_G = 0$ (Fig. 6d).

5.2 Choice of mother wavelet and decomposition depth

Fifteen mother wavelets were compared on the 378 fault records that contain at least one sound phase. Every high-pass analysis filter was first scaled to unit energy, and

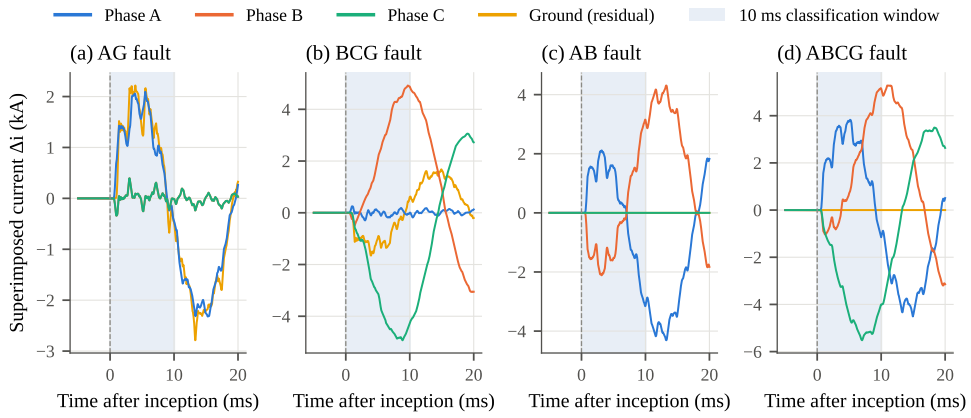


Fig. 7 Superimposed currents $\Delta i_x(\mathrm{t}) = i_x(\mathrm{t}) - i_x(\mathrm{t} - \mathrm{T})$ for the faults of Fig. 6 (200 km, $R_f = 10$ Ω); the shaded band is the 10 ms classification window

each wavelet was scored by dividing the smallest faulted phase D1 maximum by the largest sound phase maximum. Fig. 8 shows that the median ratios lie between 2.6 and 4.0 (bior5.5: 2.96), while the worst case ratios lie between 0.55 and 0.90 (bior5.5: 0.71). No wavelet reaches a worst case ratio above one, which means that no wavelet separates every faulted phase from every healthy phase on raw D1 magnitudes; the spread between wavelets is small compared with this common limitation. The bior5.5 wavelet, whose symmetric filters give linear phase, was retained for the rest of the study.

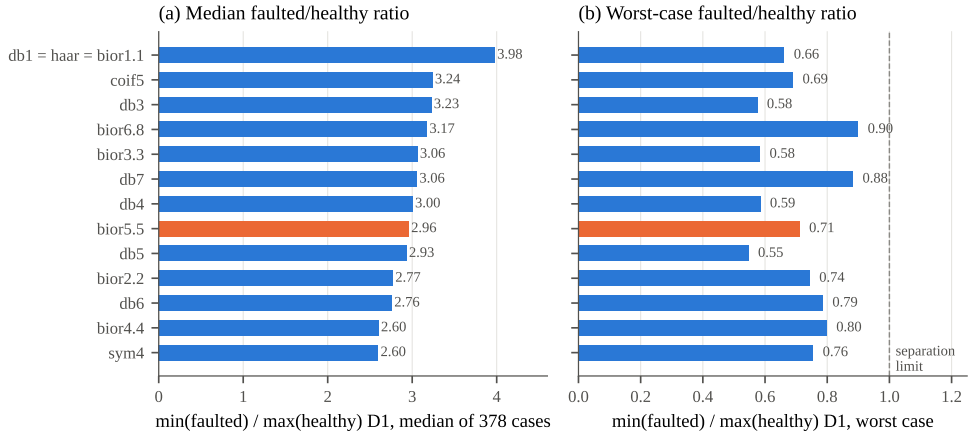


Fig. 8 Discrimination of 15 mother wavelets with unit energy filters: (a) median and (b) worst case ratio of the weakest faulted phase to the strongest healthy phase D1 maximum over 378 cases. db1, haar and bior1.1 are the same wavelet

The decomposition depth was chosen by examining how the signal energy is distributed over the levels and how strongly each level reacts to a fault (Table 4, Fig. 9). D1 carries less than 0.01 % of the current energy, yet its energy gain (the energy after the fault divided by the energy before it) is the largest of all levels for faults at 50 and 200 km (7138 and 4209). For the fault at 350 km, D5 (312–625 Hz) becomes the most sensitive level (5744 against 3452 for D1), because the line attenuates the highest frequencies over longer distances. D1 also has the shortest filter delay and needs only one filtering stage, which makes it the preferred level for fast detection.

Table 4 Distribution of energy over the decomposition levels and their response to an AG fault (current i_A, $R_f = 10\ \Omega$, windows of two cycles).

Level	Frequency range	Share of energy, 50 km (%)	Energy gain, 50 km	Energy gain, 200 km	Energy gain, 350 km
D1	5–10 kHz	0.0001	7138	4209	3452
D2	2.5–5 kHz	0.0015	3094	1324	1526
D3	1.25–2.5 kHz	0.0258	2294	349	440
D4	625–1250 Hz	0.0084	1604	2659	1359
D5	312–625 Hz	0.0236	1337	4127	5744
D6	156–312 Hz	0.1713	460	93	95
A6	0–156 Hz	99.77	—	—	—

5.3 Influence of fault type, distance and resistance on D1

For faults 200 km from the relay, Table 5 gives the largest D1 magnitude reached within 5 ms of inception for every fault type at the smallest and the largest fault resistance. Every fault raises at least one phase coefficient to between 2.0 and 22.4 A, against at most 0.39 A without a fault. The magnitudes depend strongly on the instantaneous voltage of the faulted phases at inception: phase A is at its peak (1.0 pu) at 90° on v_A, while phases B and C are at -0.5 pu, so AG faults give the largest L-G coefficients and CG faults the smallest. BC faults, incepted at the B–C voltage zero, give coefficients of only 2.0–2.6 A.

Raising R_f from 10 to 60 Ω reduces the faulted phase D1 maximum of L-G faults by 16–30 % (Fig. 10a) and their superimposed current by 37–49 % (Fig. 10b). The superimposed current falls smoothly with distance, from 4.0 kA at 50 km to 1.0 kA at 350 km for $R_f = 10\ \Omega$, whereas the D1 maximum is not monotonic: it dips at 250 km and rises again at 300 km. This behaviour is consistent with wavefront reflections between the fault, the line terminals and the π-segments, and it shows that D1 magnitudes are a weaker indicator of fault severity than the superimposed fundamental frequency current.

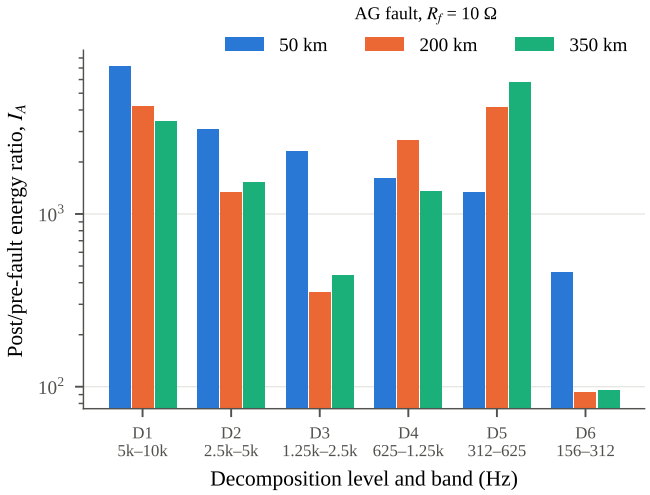


Fig. 9 Energy gain (energy after the fault over energy before the fault of i_A) at each decomposition level for AG faults with $R_f = 10\ \Omega$ located at 50, 200 and 350 km; logarithmic axis

Table 5 Peak D1 magnitudes (A) of the relay currents within 5 ms of inception for faults 200 km from the relay; Z denotes $d_A + d_B + d_C + d_G$.

	$R_f = 10\,\Omega$					$R_f = 60\,\Omega$				
Fault	d_A	d_B	d_C	d_G	Z	d_A	d_B	d_C	d_G	Z
NF	0.06	0.35	0.39	0.00	0.80	0.06	0.35	0.39	0.00	0.80
AG	13.79	11.64	11.76	28.54	65.72	11.43	9.79	9.87	22.62	53.72
BG	7.10	8.43	7.19	17.45	40.16	5.95	6.99	6.06	13.86	32.85
CG	4.52	4.67	5.36	11.09	25.63	3.76	3.95	4.44	8.80	20.94
ABG	20.03	16.86	3.46	7.71	48.06	15.33	12.68	3.06	6.71	37.77
BCG	8.44	7.58	7.54	19.78	43.34	7.37	6.29	6.25	17.21	37.12
CAG	18.66	5.24	16.42	12.08	52.40	14.42	4.61	11.53	10.52	41.08
AB	18.04	18.06	0.39	0.00	36.49	13.60	13.63	0.39	0.00	27.62
BC	0.06	2.55	2.57	0.00	5.18	0.06	1.97	1.99	0.00	4.02
CA	15.56	0.35	15.54	0.00	31.46	11.74	0.35	11.73	0.00	23.82
ABC	22.40	13.70	8.80	0.00	44.90	16.90	10.34	6.67	0.00	33.90
ABCG	22.40	13.70	8.80	0.00	44.90	16.90	10.34	6.67	0.00	33.90

5.4 Detection results

On signals without noise, the D1 detector flagged each of the 462 faults and never tripped on a healthy window. The threshold learned on the R_f-split training set is α = 0.83 A, with a margin of 4.1: the largest healthy window coefficient is 0.41 A and the smallest fault coefficient 1.56 A. The location split gives nearly the same threshold (0.83 A, margin 4.2).

How quickly a fault is flagged depends on how long the fault-generated wave takes to reach the relay (Table 6, Fig. 11). It grows linearly with distance, from 0.27 ms at 50 km to 1.50 ms at 350 km, and exceeds the travel time of Eq. (14) by 0.10–0.30 ms.

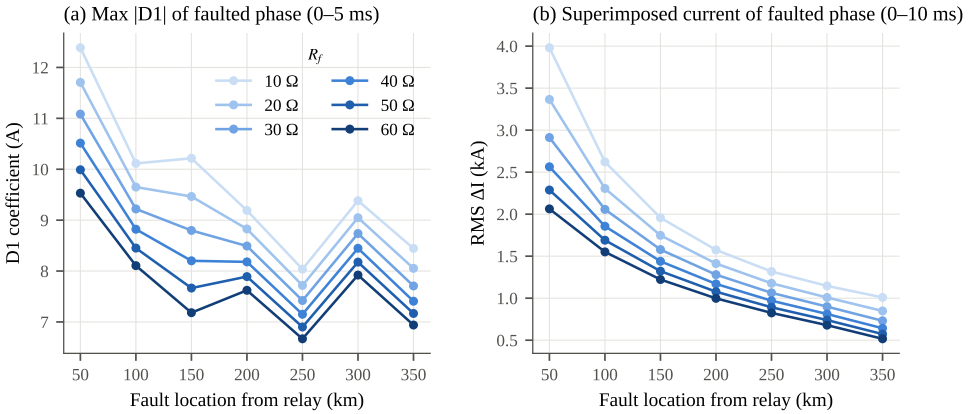


Fig. 10 Dependence on distance and fault resistance for phase-to-earth faults (average of AG, BG and CG): (a) peak |D1| of the faulted phase within 0–5 ms; (b) RMS superimposed current of the faulted phase within 0–10 ms

This offset agrees with the group delay of the symmetric bior5.5 filter with 11 taps, 5 samples $\times$ 50 μs = 0.25 ms. Over all cases the mean detection time is 0.91 ms and the maximum 1.75 ms, well within the first quarter cycle. An example worked through one sample at a time is given in Appendix A, and the detection time of every fault is listed in Appendix B.

Table 6 Time from inception to D1 detection, 66 faults at each distance.

Distance (km)	Average (ms)	Shortest (ms)	Longest (ms)	Wave delay ℓ/v (ms)	Average minus wave delay (ms)
50	0.27	0.15	0.45	0.17	0.10
100	0.52	0.45	0.65	0.34	0.18
150	0.72	0.65	0.85	0.52	0.21
200	0.93	0.85	1.15	0.69	0.24
250	1.11	0.95	1.35	0.86	0.24
300	1.29	1.15	1.55	1.04	0.25
350	1.50	1.35	1.75	1.21	0.30

Fig. 12 resolves the mean detection time by fault type and location. The spread between fault types at a given location is at most 0.40 ms. On average, faults that leave phase A healthy (BG, CG, BCG and BC) are flagged 0.18–0.28 ms later than multiphase faults that include phase A, because phases B and C sit at -0.5 pu at inception and launch weaker transients whose D1 coefficients cross α later in the wavefront. Even so, no fault takes longer than 1.75 ms to be detected.

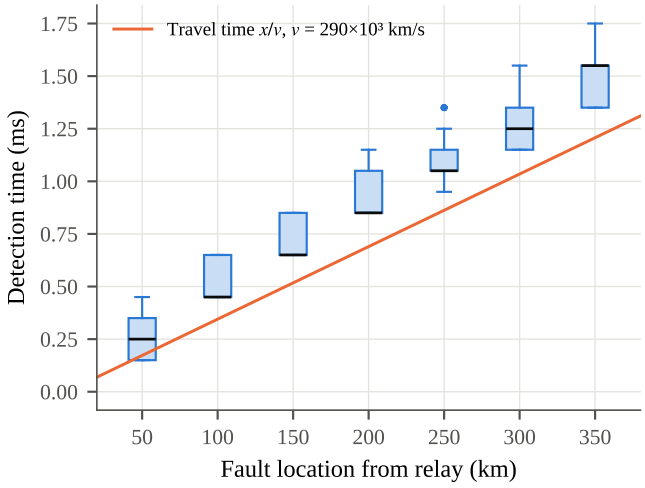


Fig. 11 Spread of the D1 detection time across fault types and resistances at each distance; the straight line is the wave delay ℓ/v with v = 2.90 $\times 10^5$ km/s

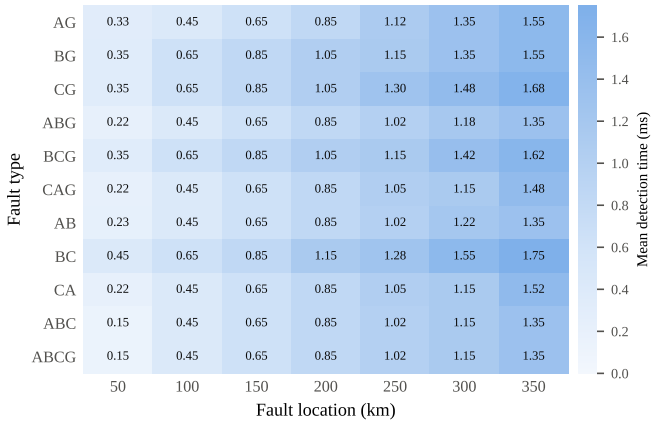


Fig. 12 Average D1 detection time (ms) for every combination of fault type and distance

5.5 Typing results

Fig. 13 explains why typing relies on the superimposed currents. On the D1 ground ratio $d_G/\max(d_A, d_B, d_C)$ (horizontal axis), BCG faults (1.91–2.57) fall inside the cluster of L-G faults (1.78–2.60), so D1 magnitudes alone cannot distinguish them. On the superimposed current ground ratio g of Eq. (9) (vertical axis), every grounded fault lies at 0.27 or above and every ungrounded or balanced fault at exactly zero. In addition, the normalised superimposed current r_x of Eq. (8) is at least 0.59 for every faulted phase and at most 0.28 for every healthy phase, so the number of faulted phases is never ambiguous.

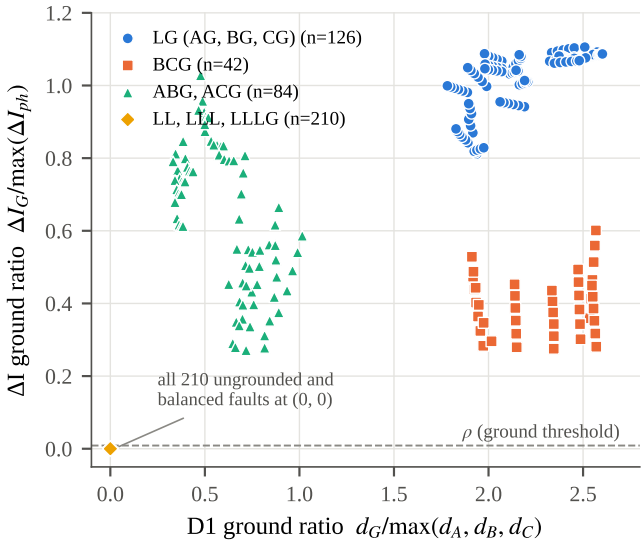


Fig. 13 Earth involvement indicators for all 462 faults: D1 ground ratio on the horizontal axis and superimposed current ground ratio g on the vertical axis; the dashed line is the fitted threshold ρ

Fig. 14 shows the distributions of the two classification features over all 462 faults. The normalised superimposed current r_x of the 504 healthy phases stays below 0.28, and that of the 882 faulted phases above 0.59, leaving a clear gap around the learned threshold $\kappa = 0.398$. The ground ratio g is exactly zero for all 210 ungrounded and balanced faults and at least 0.27 for all 252 grounded faults.

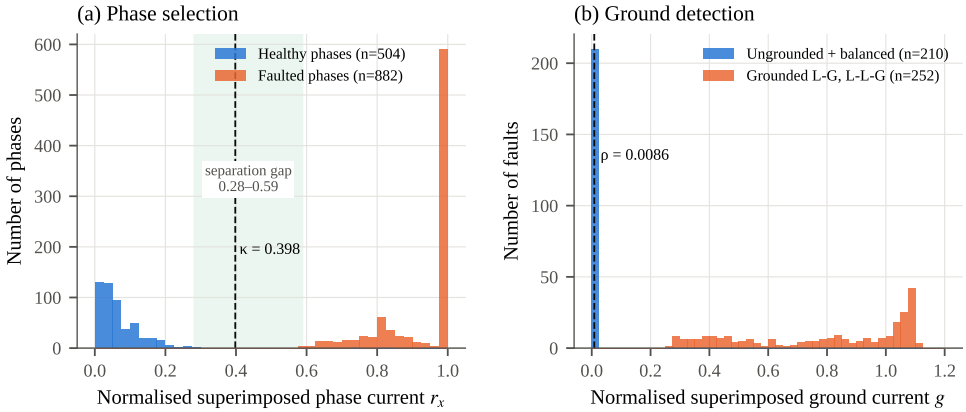


Fig. 14 Histograms of the typing indicators over all 462 faults: (a) r_x for sound and faulted phases; (b) g for faults with and without earth. Dashed lines show the fitted thresholds

Table 7 reports the thresholds fitted on the R_f-split training cases together with their margins. Every margin is above 2, so the training classes are separated with wide headroom; the ground threshold ρ has an unbounded margin in the simulated data because ungrounded faults produce no residual superimposed current.

Table 7 Fitted thresholds (R_f split) and their separation margins.

Symbol	Compared quantity	Fitted value	Margin μ
α	max $\lvert d_1 \rvert$ of the phase currents (A)	0.828	4.11
κ	normalised superimposed phase current r_x	0.398	2.18
ρ	normalised superimposed residual current g	0.0086	∞ (g = 0 for ungrounded faults)

Table 8 collects the typing accuracies obtained on the withheld cases. The proposed scheme classified every test fault correctly when ABC and ABCG are treated as one three-phase class, on both the R_f split (232 test cases) and the location split (199 test cases). With eleven separate classes, its accuracy is 90.9 % and 91.0 %; the only errors are the ABCG test faults labelled ABC, which are electrically identical in this system. The random forest and SVM trained on the 14 D1 features also reached 100 % on clean data, which shows that the level-1 coefficients do contain the classification information when they are combined in a learned, multivariate decision; their behaviour under noise is examined in Section 5.6. Because all faults share one inception angle, the learned classifiers may partly exploit patterns specific to the inception angle, which is a further reason to prefer the physically interpretable superimposed current rules. With no error among 232 (R_f split) and 199 (location split) test cases, the one-sided 95 % lower confidence bound on the accuracy with merged classes is about 98.7 % and 98.5 %, respectively (rule of three).

Table 8 Typing accuracy (%) on cases excluded from fitting.

Method	Inputs	R_f split (232 cases)	Location split (199 cases)
Random forest (500 trees)[46]	14 D1 features	100.0*	100.0*
SVM, RBF kernel[47]	14 D1 features	100.0*	100.0*
Proposed scheme, ABC ≡ ABCG	D1 detection + ΔI	100.0	100.0
Proposed scheme, 11 classes	D1 detection + ΔI	90.9	91.0

Accuracy per fault type appears in Table 9 and the corresponding confusion matrices in Fig. 15. Apart from ABCG, every fault type is typed correctly in both splits,

whatever the fault resistance or distance. The classification output of every simulated fault is listed in Tables B1 and B2.

Table 9 Typing accuracy (%) per fault type on the withheld cases.

Fault group	R_f split: cases	R_f split: correct (%)	Location split: cases	Location split: correct (%)
AG, BG, CG	21 each	100	18 each	100
ABG, BCG, CAG	21 each	100	18 each	100
AB, BC, CA	21 each	100	18 each	100
ABC	21	100	18	100
ABCG (11 classes)	21	0 (labelled ABC)	18	0 (labelled ABC)
ABCG (ABC ≡ ABCG)	21	100	18	100
No fault	1	100	1	100

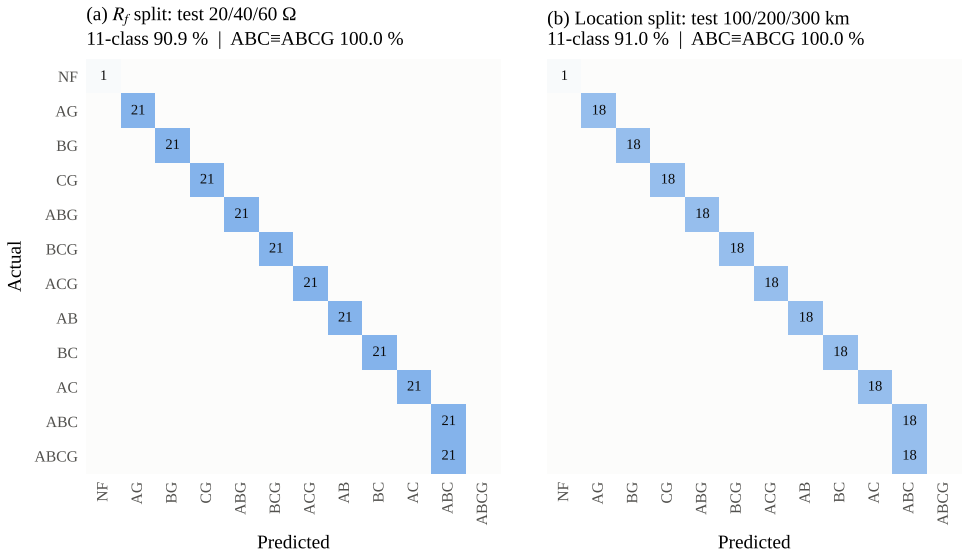


Fig. 15 Confusion matrices of the proposed scheme for (a) the R_f-split test cases and (b) the location split test cases

5.6 Behaviour under measurement noise

Results with white Gaussian noise added to the measurements are given in Table 10 and Fig. 16; all thresholds and models were refitted at every SNR. The superimposed current stage proved highly robust: as a detector it identified 97–100 % of the faults with no false trip down to 20 dB, and as a classifier it kept 100 % accuracy (ABC ≡ ABCG) at every SNR. The D1 stage is much more sensitive. At 60 dB it detected 81 % of the faults with 29 false trips among 233 healthy windows; at 30 dB and below the learned threshold tripped on every healthy window. The accuracy of the random forest on D1 features fell from 100 % to 93 % at 50 dB and to about 78 % at 40 dB and below.

Table 10 Results with noisy measurements (R_f split: 231 test faults, 233 healthy windows).

SNR (dB)	Faults found by D1 (%)	Spurious D1 trips	Faults found by ΔI (%)	Spurious ΔI trips	Random forest, D1 inputs (%)	Proposed typing (%)
Clean	100.0	0	100.0	0	100.0	100.0
60	81.0	29	100.0	0	100.0	100.0
50	66.7	101	100.0	0	93.1	100.0
40	74.5	182	100.0	0	77.5	100.0
30	100.0	231	100.0	0	77.9	100.0
20	100.0	231	97.0	0	77.9	100.0

Classification accuracies assume that the fault has been detected and treat ABC and ABCG as one class. The location split gives the same picture: the random forest on D1 features falls to 78–80 % at 40 dB and below, while the proposed classifier stays at 100 %.

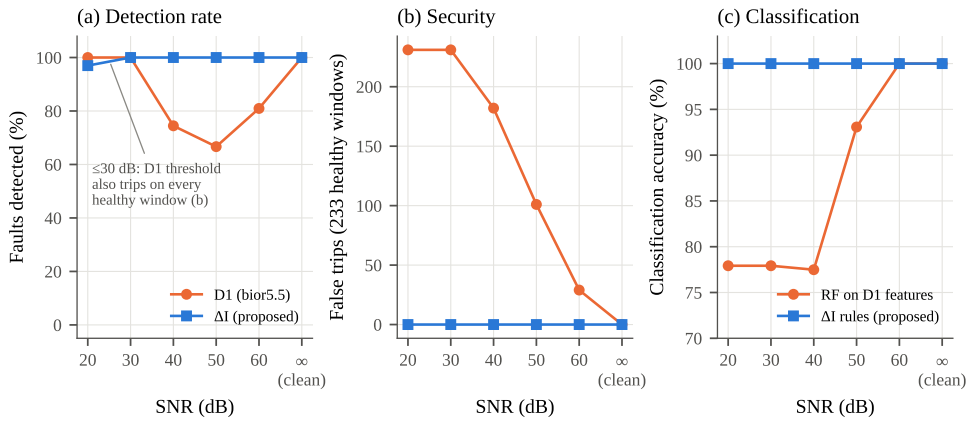


Fig. 16 Influence of measurement noise (R_f split): (a) share of faults detected, (b) spurious trips in healthy windows, (c) typing accuracy

The difference between the two stages follows from the size of the signatures. The largest D1 coefficient of a fault is only 1.6–42 A, a median of 0.8 % of the superimposed fault current, while white noise spreads evenly over the spectrum: in a healthy window its D1 maxima reach a median of 4.7 A at 60 dB, 150 A at 30 dB and 470 A at 20 dB. The superimposed current, in contrast, integrates the fault signal over half a cycle in the low frequency band where most of its energy lies. In a noisy environment, the D1 trigger should therefore be confirmed by the superimposed current detector, or the measurement chain should provide an SNR above about 60 dB in the 5–10 kHz band.

5.7 Computing effort and relay implementation

The computing effort is modest enough for a numerical relay. The level-1 bior5.5 filter needs 11 multiply and add operations per output coefficient and phase at 10 kHz (the downsampled rate), and the superimposed currents need one subtraction and one squaring and accumulation per sample and signal at 20 kHz, with a buffer of 400 samples per channel. The decision is available half a cycle after the fault, so that, with a maximum detection time of 1.75 ms, the fault type is known within 11.75 ms of inception. Table 11 summarises the performance indices of the proposed scheme.

Table 11 Key performance figures of the proposed scheme.

Performance measure	Result
Detection time (mean / maximum)	0.91 ms / 1.75 ms
Detection time at 50 km / 350 km (mean)	0.27 ms / 1.50 ms
Missed faults / false trips (clean data)	0 / 0
Classification window	10 ms (half cycle)
Classification accuracy, ABC ≡ ABCG (R_f / location split)	100 % / 100 %
Classification accuracy, 11 classes (R_f / location split)	90.9 % / 91.0 %
Superimposed current detection at 20 dB SNR	97.0 %, no false trips
Classification accuracy at 20 dB SNR	100 %
Operations per sample and phase	11 multiply and add (D1, at 10 kHz) + 2 (ΔI, at 20 kHz)

5.8 Scope of the study

The findings refer to an uncompensated 400 kV line, faults switched in at 90° of the phase A voltage, ideal current sensing and a line represented by cascaded 5 km π-segments. Inside these bounds the scheme behaved as described above, and four extensions would broaden its validity:

- further fault inception angles, because the size of the level-1 transient depends on the instantaneous voltage when the fault occurs;

- models of current transformers and antialiasing filters, together with a distributed-parameter line, to confirm the D1 magnitudes in the 5–10 kHz band;
- series-compensated lines and different source strengths;
- nonfault switching events, such as load and capacitor switching, to confirm the security of the D1 trigger beyond steady state healthy windows.

Because a symmetrical fault drives no zero-sequence current, ABC and ABCG faults produce identical relay currents here and are reported as a single three-phase class; this is all the information needed for tripping and autoreclosing.

6 Conclusion

A two-stage relaying principle was developed for a 400 kV, 50 Hz, 400 km line and assessed with 462 simulated faults that span eleven fault types, seven distances between 50 and 350 km and six fault resistances between 10 and 60 Ω. In the first stage, level-1 bior5.5 detail coefficients flagged every fault with no spurious trip; the average delay of 0.27–1.50 ms equals the wave travel time to the relay plus the 0.25 ms group delay of the filter. Inspection of the 5–10 kHz transient revealed that the ground mode dominates in phase-to-earth faults and in BCG faults switched in at the B–C voltage zero, which makes D1 magnitudes unreliable for naming the faulted phases. The second stage therefore types the fault from the half cycle RMS values of the superimposed phase and residual currents, with thresholds fitted on training cases. On fault resistances and distances withheld from fitting, every fault was typed correctly once the physically identical ABC and ABCG faults are merged into one class (90.9–91.0 % with eleven separate classes), and the superimposed current stage kept this accuracy, without spurious trips, down to an SNR of 20 dB, whereas the wavelet trigger required an SNR above about 60 dB and should be confirmed by the superimposed current detector in noisy conditions. Because only one filtering stage and simple arithmetic are needed, the principle is well suited to numerical relays. Further work will cover additional inception angles, distributed-parameter line models, series-compensated lines, instrument transformer models and hardware-in-the-loop testing.

Supplementary information. ESM 1 (ESM_1_Supplementary_Data_Tables.xlsx): Excel workbook that reproduces Tables 2–11 and the appendix tables and lists the features extracted from all 463 simulated cases. ESM 2 (ESM_2_Supplementary_Code.zip): MATLAB scripts for running the simulations, extracting the features and classifying the faults, and Python scripts for the analysis and figures.

Declarations

- **Funding:** No funding was received for this work.
- **Competing interests:** The authors have no competing interests to declare.
- **Ethics approval and consent to participate:** Not applicable. The work relies solely on computer simulation and involves no human participants, human data or animals.
- **Consent for publication:** Not applicable.

- **Data availability:** The authors generated every dataset used in this work. Fault records were obtained by simulating the 400 kV, 400 km network of Section 3 in MATLAB/Simulink (Simscape Electrical) for 462 fault conditions and one healthy condition, and the features and results were derived from these records with the procedures of Section 4. No external or third party data were involved. The MATLAB simulation data supporting the findings of this study, namely the sampled relay currents (i_A, i_B, i_C; 20 kHz) of all 463 simulated cases with a case index giving the fault type, distance, fault resistance, inception sample and detection time of each case, are openly available at https://sites.google.com/dr.sharda.ac.in/data-set-abhay-a-hybrid-biorth/home. The tables, figures and appendices of the article and the Supplementary Data Tables (ESM 1) also contain data that support the findings.
- **Materials availability:** Not applicable.
- **Author contribution:** Abhay Yadav conceived the study, built the simulation model, generated the data, developed the method, carried out the analysis, prepared the figures and wrote the first draft. Soma Deb supervised the work, contributed to the method, validated the results and revised the manuscript. Both authors have read and agreed to the final version.

Appendix A Worked calculation of the detection and classification process

This appendix shows, for four representative test faults, how the scheme of Section 4 turns the sampled relay currents into a trip decision. All four faults are at 200 km with $R_f = 20\ \Omega$, a fault resistance that was not used for training. The settings are those learned on the R_f-split training set (Table A1).

Table A1 Settings of the proposed scheme used in the appendix calculations.

Quantity	Symbol	Value
Sampling frequency / period	f_s / T_s	20 kHz / 50 μs
Samples per fundamental cycle	N	400
Wavelet and level	—	bior5.5, level 1 (D1: 5–10 kHz)
Detection threshold	α	0.828 A
Detection window	W_d	5 ms (100 D1 coefficients)
Classification window	W_c	10 ms (M = 200 samples)
Phase selection threshold	κ	0.398
Ground threshold	ρ	0.0086
Propagation velocity, aerial / ground mode	v_1 / v_0	2.90 $\times 10^5$ / 1.77 $\times 10^5$ km/s

A.1 Detection: D1 coefficients sample by sample

Table A2 lists the level-1 detail coefficients of the AG fault from just before inception to the detection instant. The coefficients stay at the numerical noise level (below 0.25 A) until the first aerial mode wavefront arrives, 0.69 ms after inception (200 km / v_1). The first coefficient that exceeds $\alpha = 0.828$ A appears at 0.85 ms ($d_A = 1.20$ A); this is the detection instant. The residual coefficient d_G stays small until about 1.13 ms, when the slower ground mode wave (200 km / v_0) arrives.

Table A2 Level-1 bior5.5 detail coefficients (A) around the detection instant, AG fault at 200 km, $R_f = 20\ \Omega$. Time is measured from fault inception; one D1 coefficient every 0.1 ms.

t (ms)	d_A	d_B	d_C	d_G	max$\lvert d_{ph}\rvert$	max$\lvert d_{ph}\rvert$ ¿ α ?
-0.15	0.02	0.12	-0.15	-0.00	0.15	No
-0.05	0.00	-0.03	0.02	-0.00	0.03	No
0.05	-0.01	-0.08	0.09	-0.00	0.09	No
0.15	-0.02	-0.06	0.08	-0.00	0.08	No
0.25	0.01	0.13	-0.15	-0.00	0.15	No
0.35	0.01	0.02	-0.03	-0.00	0.03	No
0.45	-0.01	-0.01	0.02	-0.00	0.02	No
0.55	-0.07	-0.12	0.19	-0.00	0.19	No
0.65	-0.12	0.12	0.00	-0.00	0.12	No
0.75	0.23	-0.02	-0.20	-0.00	0.23	No
0.85	1.20	-0.54	-0.67	-0.01	1.20	Yes, fault detected
0.95	-1.39	0.52	0.81	-0.07	1.39	Yes, fault detected
1.05	-3.45	1.54	1.77	-0.14	3.45	Yes, fault detected
1.15	7.00	-3.16	-3.66	0.18	7.00	Yes, fault detected

A.2 Classification: superimposed current calculation

Table A3 follows the four faults through the classification stage. The RMS superimposed currents of Eq. (7) are computed over the 10 ms window, normalised by the largest phase value with Eqs. (8) and (9), and compared with κ and ρ. The decision is issued at the end of the classification window, so the response time of the scheme is the detection time plus 10 ms.

For the AG fault only r_A exceeds κ, so a single-phase fault with ground is declared. For the BCG fault, $r_B = 0.834$ and $r_C = 1.000$ exceed κ while $r_A = 0.038$ does not, and g = 0.310 ¿ ρ confirms ground involvement, even though its D1 pattern resembles that of an L-G fault. For the AB fault g = 0, indicating an ungrounded fault, and for the ABCG fault all three phases exceed κ, giving the three-phase class.

Appendix B Detection time and classification result of all simulated faults

Tables B1 and B2 list the D1 detection time and the output of the classifier for each of the 462 simulated faults, using the R_f-split settings of Table A1. Cases with $R_f =$ 10, 30 and 50 Ω belong to the training set and cases with $R_f = 20$, 40 and 60 Ω to the

Table A3 Detection and classification of four test faults, step by step at 200 km, $R_f = 20\ \Omega$.

Step	AG	BCG	AB	ABCG
Wave travel time ℓ/v_1 (ms)	0.69	0.69	0.69	0.69
Detection time t_{det} (ms)	0.85	1.05	0.85	0.85
$\max\|d_{ph}\|$ at t_{det} (A)	1.20	1.30	2.19	2.74
Healthy window $\max\|d_{ph}\|$ (A)	0.41	0.41	0.41	0.41
ΔI_A (kA rms)	1.150	0.104	1.431	1.989
ΔI_B (kA rms)	0.126	2.304	1.431	2.225
ΔI_C (kA rms)	0.126	2.762	0.000	3.101
ΔI_G (kA rms)	1.233	0.856	0.000	0.000
$r_A = \Delta I_A$ / max ΔI_{ph}	1.000	0.038	1.000	0.641
$r_B = \Delta I_B$ / max ΔI_{ph}	0.109	0.834	1.000	0.717
$r_C = \Delta I_C$ / max ΔI_{ph}	0.109	1.000	0.000	1.000
g = ΔI_G / max ΔI_{ph}	1.072	0.310	0.000	0.000
Faulted phases (r_x ¿ κ)	A	BC	AB	ABC
Ground involvement	Yes (one phase)	Yes (g ¿ ρ)	No (g $\leq \rho$)	Not needed (three phases)
Classified as	AG	BCG	AB	ABC/ABCG
Response time t_{det} + 10 ms (ms)	10.85	11.05	10.85	10.85

test set. Every fault is detected, and every predicted class equals the true fault type, except that ABCG faults are reported as the equivalent three-phase class ABC.

Table B3 summarises the detection and classification margins at each fault location. The smallest fault D1 coefficient is at least 1.56 A, against a largest healthy window value of 0.41 A, and the faulted and healthy normalised superimposed currents remain separated at every location.

Appendix C Response time budget and computational steps

Table C1 breaks the response of the scheme into its sequential steps, from fault inception to the classification output. The breaker opening time is not included.

Table B1 D1 detection time (ms) / classified fault type for the 252 earth faults (L-G and L-L-G). Training cases: R_f = 10, 30, 50 Ω; test cases: R_f = 20, 40, 60 Ω.

Fault	Loc. (km)	R_f = 10 Ω	R_f = 20 Ω	R_f = 30 Ω	R_f = 40 Ω	R_f = 50 Ω	R_f = 60 Ω
AG	50	0.25/AG	0.35/AG	0.35/AG	0.35/AG	0.35/AG	0.35/AG
AG	100	0.45/AG	0.45/AG	0.45/AG	0.45/AG	0.45/AG	0.45/AG
AG	150	0.65/AG	0.65/AG	0.65/AG	0.65/AG	0.65/AG	0.65/AG
AG	200	0.85/AG	0.85/AG	0.85/AG	0.85/AG	0.85/AG	0.85/AG
AG	250	1.05/AG	1.05/AG	1.15/AG	1.15/AG	1.15/AG	1.15/AG
AG	300	1.35/AG	1.35/AG	1.35/AG	1.35/AG	1.35/AG	1.35/AG
AG	350	1.55/AG	1.55/AG	1.55/AG	1.55/AG	1.55/AG	1.55/AG
BG	50	0.35/BG	0.35/BG	0.35/BG	0.35/BG	0.35/BG	0.35/BG
BG	100	0.65/BG	0.65/BG	0.65/BG	0.65/BG	0.65/BG	0.65/BG
BG	150	0.85/BG	0.85/BG	0.85/BG	0.85/BG	0.85/BG	0.85/BG
BG	200	1.05/BG	1.05/BG	1.05/BG	1.05/BG	1.05/BG	1.05/BG
BG	250	1.15/BG	1.15/BG	1.15/BG	1.15/BG	1.15/BG	1.15/BG
BG	300	1.35/BG	1.35/BG	1.35/BG	1.35/BG	1.35/BG	1.35/BG
BG	350	1.55/BG	1.55/BG	1.55/BG	1.55/BG	1.55/BG	1.55/BG
CG	50	0.35/CG	0.35/CG	0.35/CG	0.35/CG	0.35/CG	0.35/CG
CG	100	0.65/CG	0.65/CG	0.65/CG	0.65/CG	0.65/CG	0.65/CG
CG	150	0.85/CG	0.85/CG	0.85/CG	0.85/CG	0.85/CG	0.85/CG
CG	200	1.05/CG	1.05/CG	1.05/CG	1.05/CG	1.05/CG	1.05/CG
CG	250	1.25/CG	1.25/CG	1.25/CG	1.35/CG	1.35/CG	1.35/CG
CG	300	1.35/CG	1.35/CG	1.55/CG	1.55/CG	1.55/CG	1.55/CG
CG	350	1.55/CG	1.55/CG	1.75/CG	1.75/CG	1.75/CG	1.75/CG
ABG	50	0.15/ABG	0.15/ABG	0.25/ABG	0.25/ABG	0.25/ABG	0.25/ABG
ABG	100	0.45/ABG	0.45/ABG	0.45/ABG	0.45/ABG	0.45/ABG	0.45/ABG
ABG	150	0.65/ABG	0.65/ABG	0.65/ABG	0.65/ABG	0.65/ABG	0.65/ABG
ABG	200	0.85/ABG	0.85/ABG	0.85/ABG	0.85/ABG	0.85/ABG	0.85/ABG
ABG	250	0.95/ABG	0.95/ABG	1.05/ABG	1.05/ABG	1.05/ABG	1.05/ABG
ABG	300	1.15/ABG	1.15/ABG	1.15/ABG	1.15/ABG	1.15/ABG	1.35/ABG
ABG	350	1.35/ABG	1.35/ABG	1.35/ABG	1.35/ABG	1.35/ABG	1.35/ABG
BCG	50	0.35/BCG	0.35/BCG	0.35/BCG	0.35/BCG	0.35/BCG	0.35/BCG
BCG	100	0.65/BCG	0.65/BCG	0.65/BCG	0.65/BCG	0.65/BCG	0.65/BCG
BCG	150	0.85/BCG	0.85/BCG	0.85/BCG	0.85/BCG	0.85/BCG	0.85/BCG
BCG	200	1.05/BCG	1.05/BCG	1.05/BCG	1.05/BCG	1.05/BCG	1.05/BCG
BCG	250	1.15/BCG	1.15/BCG	1.15/BCG	1.15/BCG	1.15/BCG	1.15/BCG
BCG	300	1.35/BCG	1.35/BCG	1.35/BCG	1.35/BCG	1.55/BCG	1.55/BCG
BCG	350	1.55/BCG	1.55/BCG	1.55/BCG	1.55/BCG	1.75/BCG	1.75/BCG
CAG	50	0.15/ACG	0.15/ACG	0.25/ACG	0.25/ACG	0.25/ACG	0.25/ACG
CAG	100	0.45/ACG	0.45/ACG	0.45/ACG	0.45/ACG	0.45/ACG	0.45/ACG
CAG	150	0.65/ACG	0.65/ACG	0.65/ACG	0.65/ACG	0.65/ACG	0.65/ACG
CAG	200	0.85/ACG	0.85/ACG	0.85/ACG	0.85/ACG	0.85/ACG	0.85/ACG
CAG	250	1.05/ACG	1.05/ACG	1.05/ACG	1.05/ACG	1.05/ACG	1.05/ACG
CAG	300	1.15/ACG	1.15/ACG	1.15/ACG	1.15/ACG	1.15/ACG	1.15/ACG
CAG	350	1.35/ACG	1.35/ACG	1.55/ACG	1.55/ACG	1.55/ACG	1.55/ACG

Table B2 D1 detection time (ms) / classified fault type for the 210 line-to-line and three-phase faults (AB, BC, CA, ABC, ABCG). Training cases: R_f = 10, 30, 50 Ω; test cases: R_f = 20, 40, 60 Ω.

Fault	Loc. (km)	$R_f = 10\ \Omega$	$R_f = 20\ \Omega$	$R_f = 30\ \Omega$	$R_f = 40\ \Omega$	$R_f = 50\ \Omega$	$R_f = 60\ \Omega$
AB	50	0.15/AB	0.25/AB	0.25/AB	0.25/AB	0.25/AB	0.25/AB
AB	100	0.45/AB	0.45/AB	0.45/AB	0.45/AB	0.45/AB	0.45/AB
AB	150	0.65/AB	0.65/AB	0.65/AB	0.65/AB	0.65/AB	0.65/AB
AB	200	0.85/AB	0.85/AB	0.85/AB	0.85/AB	0.85/AB	0.85/AB
AB	250	0.95/AB	0.95/AB	1.05/AB	1.05/AB	1.05/AB	1.05/AB
AB	300	1.15/AB	1.15/AB	1.15/AB	1.15/AB	1.35/AB	1.35/AB
AB	350	1.35/AB	1.35/AB	1.35/AB	1.35/AB	1.35/AB	1.35/AB
BC	50	0.45/BC	0.45/BC	0.45/BC	0.45/BC	0.45/BC	0.45/BC
BC	100	0.65/BC	0.65/BC	0.65/BC	0.65/BC	0.65/BC	0.65/BC
BC	150	0.85/BC	0.85/BC	0.85/BC	0.85/BC	0.85/BC	0.85/BC
BC	200	1.15/BC	1.15/BC	1.15/BC	1.15/BC	1.15/BC	1.15/BC
BC	250	1.15/BC	1.15/BC	1.35/BC	1.35/BC	1.35/BC	1.35/BC
BC	300	1.55/BC	1.55/BC	1.55/BC	1.55/BC	1.55/BC	1.55/BC
BC	350	1.75/BC	1.75/BC	1.75/BC	1.75/BC	1.75/BC	1.75/BC
CA	50	0.15/AC	0.15/AC	0.25/AC	0.25/AC	0.25/AC	0.25/AC
CA	100	0.45/AC	0.45/AC	0.45/AC	0.45/AC	0.45/AC	0.45/AC
CA	150	0.65/AC	0.65/AC	0.65/AC	0.65/AC	0.65/AC	0.65/AC
CA	200	0.85/AC	0.85/AC	0.85/AC	0.85/AC	0.85/AC	0.85/AC
CA	250	1.05/AC	1.05/AC	1.05/AC	1.05/AC	1.05/AC	1.05/AC
CA	300	1.15/AC	1.15/AC	1.15/AC	1.15/AC	1.15/AC	1.15/AC
CA	350	1.35/AC	1.55/AC	1.55/AC	1.55/AC	1.55/AC	1.55/AC
ABC	50	0.15/ABC	0.15/ABC	0.15/ABC	0.15/ABC	0.15/ABC	0.15/ABC
ABC	100	0.45/ABC	0.45/ABC	0.45/ABC	0.45/ABC	0.45/ABC	0.45/ABC
ABC	150	0.65/ABC	0.65/ABC	0.65/ABC	0.65/ABC	0.65/ABC	0.65/ABC
ABC	200	0.85/ABC	0.85/ABC	0.85/ABC	0.85/ABC	0.85/ABC	0.85/ABC
ABC	250	0.95/ABC	0.95/ABC	1.05/ABC	1.05/ABC	1.05/ABC	1.05/ABC
ABC	300	1.15/ABC	1.15/ABC	1.15/ABC	1.15/ABC	1.15/ABC	1.15/ABC
ABC	350	1.35/ABC	1.35/ABC	1.35/ABC	1.35/ABC	1.35/ABC	1.35/ABC
ABCG	50	0.15/ABC	0.15/ABC	0.15/ABC	0.15/ABC	0.15/ABC	0.15/ABC
ABCG	100	0.45/ABC	0.45/ABC	0.45/ABC	0.45/ABC	0.45/ABC	0.45/ABC
ABCG	150	0.65/ABC	0.65/ABC	0.65/ABC	0.65/ABC	0.65/ABC	0.65/ABC
ABCG	200	0.85/ABC	0.85/ABC	0.85/ABC	0.85/ABC	0.85/ABC	0.85/ABC
ABCG	250	0.95/ABC	0.95/ABC	1.05/ABC	1.05/ABC	1.05/ABC	1.05/ABC
ABCG	300	1.15/ABC	1.15/ABC	1.15/ABC	1.15/ABC	1.15/ABC	1.15/ABC
ABCG	350	1.35/ABC	1.35/ABC	1.35/ABC	1.35/ABC	1.35/ABC	1.35/ABC

Table B3 Detection and classification margins at each fault location (66 faults per location).

Loc. (km)	Min fault $\max\lvert d_{ph}\rvert$ (A)	Mean t_{det} (ms)	Max t_{det} (ms)	Min r_x, faulted	Max r_x, healthy	Min g, grounded	Max g, ungrounded
50	2.07	0.27	0.45	0.588	0.084	0.359	0.000
100	1.56	0.52	0.65	0.591	0.105	0.302	0.000
150	1.70	0.72	0.85	0.601	0.129	0.281	0.000
200	1.99	0.93	1.15	0.618	0.130	0.275	0.000
250	2.33	1.11	1.35	0.636	0.178	0.279	0.000
300	2.19	1.29	1.55	0.634	0.215	0.271	0.000
350	2.21	1.50	1.75	0.679	0.283	0.278	0.000

Table C1 Response time budget of the proposed scheme.

Step	Operation	Computation	Time (ms)
1	Fault-generated wave travels to the relay	Physical propagation, ℓ/v_1	0.17 (50 km) – 1.21 (350 km)
2	Current sampling	A/D conversion at 20 kHz	0.05 per sample
3	Level-1 bior5.5 filtering	11 multiply and add operations per phase and output (10 kHz)	Group delay $\approx$ 0.25
4	Detection test	Compare max$\lvert d_{ph}\rvert$ with α (3 comparisons)	¡ 0.05
5	Detection time (steps 1–4)	Measured over all 462 faults	0.15 – 1.75 (mean 0.91)
6	Superimposed currents and RMS values	1 subtraction + 1 square and accumulate per sample and signal; buffer of 400 samples	10 (half cycle window)
7	Normalisation and decision logic	4 divisions, 4 comparisons	¡ 0.05
8	Total response time (steps 5–7)	Fault type available after inception	$\leq$ 11.75

References

[1] Chothani N, et al. Transmission line fault detection and classification using bi-orthogonal wavelet transform (5.5) based signal decomposition. Sci Rep. 2026;16:5303. https://doi.org/10.1038/s41598-026-35929-0.

[2] Chen K, Huang C, He J. Fault detection, classification and location for transmission lines and distribution systems: a review on the methods. High Volt. 2016;1(1):25–33. https://doi.org/10.1049/hve.2016.0005.

[3] Shakiba FM, Azizi SM, Zhou M, Abusorrah A. Application of machine learning methods in fault detection and classification of power transmission lines: a survey. Artif Intell Rev. 2023;56(7):5799–5836. https://doi.org/10.1007/s10462-022-10296-0.

[4] Wong SY, et al. Power transmission line fault detection and diagnosis based on artificial intelligence approach and its development in UAV: a review. Arab J Sci Eng. 2021;46(10):9305–9331. https://doi.org/10.1007/s13369-021-05522-w.

[5] Ghaderi A, Ginn HL, Mohammadpour HA. High impedance fault detection: a review. Electr Power Syst Res. 2017;143:376–388. https://doi.org/10.1016/j.epsr.2016.10.021.

[6] Arumuga M, Reddy MJB. Distance protection methodology for detection of faulted phase and fault along with power swing using apparent impedance. IEEE Access. 2022;10:43583–43597. https://doi.org/10.1109/ACCESS.2022.3168563.

[7] Unde S, Gawande P, Dambhare S. New algorithm for protection of double circuit transmission lines using modal currents. IEEE Trans Power Deliv. 2019;34(5):1967–1977. https://doi.org/10.1109/TPWRD.2019.2906939.

[8] Zheng L, Jia K, Bi T, Yang Z, Fang Y. A novel structural similarity based pilot protection for renewable power transmission line. IEEE Trans Power Deliv. 2020;35(6):2672–2681. https://doi.org/10.1109/TPWRD.2020.2973505.

[9] Yang Z, et al. High-frequency fault component-based distance protection for large renewable power plants. IEEE Trans Power Electron. 2020;35(10):10352–10362. https://doi.org/10.1109/TPEL.2020.2978266.

[10] Dong X, Kong W, Cui T. Fault classification and faulted-phase selection based on the initial current traveling wave. IEEE Trans Power Deliv. 2009;24(2):552–559. https://doi.org/10.1109/TPWRD.2008.921144.

[11] Mallat SG. A theory for multiresolution signal decomposition: the wavelet representation. IEEE Trans Pattern Anal Mach Intell. 1989;11(7):674–693. https://doi.org/10.1109/34.192463.

[12] Daubechies I. The wavelet transform, time-frequency localization and signal analysis. IEEE Trans Inf Theory. 1990;36(5):961–1005. https://doi.org/10.1109/18.57199.

[13] Priyadarshini MS, et al. Perception of power quality disturbances using Fourier, short-time Fourier, continuous and discrete wavelet transforms. Sci Rep. 2024;14:3443. https://doi.org/10.1038/s41598-024-53792-9.

[14] Cohen A, Daubechies I, Feauveau JC. Biorthogonal bases of compactly supported wavelets. Commun Pure Appl Math. 1992;45(5):485–560. https://doi.org/10.1002/cpa.3160450502.

[15] Magnago FH, Abur A. Fault location using wavelets. IEEE Trans Power Deliv. 1998;13(4):1475–1480. https://doi.org/10.1109/61.714808.

[16] Silva KM, Souza BA, Brito NSD. Fault detection and classification in transmission lines based on wavelet transform and ANN. IEEE Trans Power Deliv. 2006;21(4):2058–2063. https://doi.org/10.1109/TPWRD.2006.876659.

[17] He Z, Fu L, Lin S, Bo Z. Fault detection and classification in EHV transmission line based on wavelet singular entropy. IEEE Trans Power Deliv. 2010;25(4):2156–2163. https://doi.org/10.1109/TPWRD.2010.2042624.

[18] Costa FB. Fault-induced transient detection based on real-time analysis of the wavelet coefficient energy. IEEE Trans Power Deliv. 2014;29(1):140–153. https://doi.org/10.1109/TPWRD.2013.2278272.

[19] Megahed AI, Moussa AM, Bayoumy AE. Usage of wavelet transform in the protection of series-compensated transmission lines. IEEE Trans Power Deliv. 2006;21(3):1213–1221. https://doi.org/10.1109/TPWRD.2006.876981.

[20] Shaik AG, Pulipaka RRV. A new wavelet based fault detection, classification and location in transmission lines. Int J Electr Power Energy Syst. 2015;64:35–40. https://doi.org/10.1016/j.ijepes.2014.06.065.

[21] Abdullah A. Ultrafast transmission line fault detection using a DWT-based ANN. IEEE Trans Ind Appl. 2018;54(2):1182–1193. https://doi.org/10.1109/TIA.2017.2774202.

[22] Yusuff AA, Jimoh AA, Munda JL. Fault location in transmission lines based on stationary wavelet transform, determinant function feature and support vector regression. Electr Power Syst Res. 2014;110:73–83. https://doi.org/10.1016/j.epsr.2014.01.002.

[23] Adly AR, El Sehiemy RA, Abdelaziz AY, Ayad NMA. Critical aspects on wavelet transforms based fault identification procedures in HV transmission line. IET Gener Transm Distrib. 2016;10(2):508–517. https://doi.org/10.1049/iet-gtd.2015.

0899.

[24] Ananthan SN, et al. Real-time fault analysis of transmission lines using wavelet multi-resolution analysis based frequency-domain approach. IET Sci Meas Technol. 2016;10(7):693–703. https://doi.org/10.1049/iet-smt.2016.0038.

[25] Borghetti A, Bosetti M, Nucci CA, Paolone M, Abur A. Integrated use of time-frequency wavelet decompositions for fault location in distribution networks: theory and experimental validation. IEEE Trans Power Deliv. 2010;25(4):3139–3146. https://doi.org/10.1109/TPWRD.2010.2046655.

[26] Shalby EM, et al. A comprehensive guide to selecting suitable wavelet decomposition level and functions in discrete wavelet transform for fault detection in distribution networks. Sci Rep. 2025;15:1160. https://doi.org/10.1038/s41598-025-82025-2.

[27] Chiradeja P, Ngaopitakkul A. Identify direct lightning strike location based on discrete wavelet transform for 115-kV transmission system. IEEE Access. 2022;10:80609–80622. https://doi.org/10.1109/ACCESS.2022.3195497.

[28] Bhatnagar M, Yadav A, Swetapadma A. A resilient protection scheme for common shunt fault and high impedance fault in distribution lines using wavelet transform. IEEE Syst J. 2022;16(4):5281–5292. https://doi.org/10.1109/JSYST.2022.3172982.

[29] Bao G, Zeng F, Sun H. Design of a short-circuit detection intelligent release using discrete wavelet algorithm. IEEE Access. 2019;7:104228–104240. https://doi.org/10.1109/ACCESS.2019.2931704.

[30] Ananwattanaporn S, et al. Development of overcurrent relay based on wavelet transform for fault detection in transmission line. Sci Rep. 2024;14:14933. https://doi.org/10.1038/s41598-024-65596-y.

[31] Pei X, et al. A novel ultra-high-speed traveling-wave protection principle for VSC-based DC grids. IEEE Access. 2019;7:119765–119773. https://doi.org/10.1109/ACCESS.2019.2936276.

[32] Chatterjee B, Debnath S. A new protection scheme for transmission lines utilizing positive sequence fault components. Electr Power Syst Res. 2021;190:106847. https://doi.org/10.1016/j.epsr.2020.106847.

[33] Guillen D, et al. Fault detection and classification in transmission lines based on a PSD index. IET Gener Transm Distrib. 2018;12:4070–4078. https://doi.org/10.1049/iet-gtd.2018.5062.

[34] Vyas BY, Maheshwari RP, Das B. Versatile relaying algorithm for detection and classification of fault on transmission line. Electr Power Syst Res.

2021;192:106913. https://doi.org/10.1016/j.epsr.2020.106913.

[35] Upendar J, Gupta CP, Singh GK. Statistical decision-tree based fault classification scheme for protection of power transmission lines. Int J Electr Power Energy Syst. 2012;36(1):1–12. https://doi.org/10.1016/j.ijepes.2011.08.005.

[36] Ekici S. Support vector machines for classification and locating faults on transmission lines. Appl Soft Comput. 2012;12(6):1650–1658. https://doi.org/10.1016/j.asoc.2012.02.011.

[37] Chen YQ, Fink O, Sansavini G. Combined fault location and classification for power transmission lines fault diagnosis with integrated feature extraction. IEEE Trans Ind Electron. 2018;65(1):561–569. https://doi.org/10.1109/TIE.2017.2721922.

[38] Fahim SR, Sarker SK, Muyeen SM, Das SK, Kamwa I. A deep learning based intelligent approach in detection and classification of transmission line faults. Int J Electr Power Energy Syst. 2021;133:107102. https://doi.org/10.1016/j.ijepes.2021.107102.

[39] Belagoune S, Bali N, Bakdi A, Baadji B, Atif K. Deep learning through LSTM classification and regression for transmission line fault detection, diagnosis and location in large-scale multi-machine power systems. Measurement. 2021;177:109330. https://doi.org/10.1016/j.measurement.2021.109330.

[40] Rai P, Londhe ND, Raj R. Fault classification in power system distribution network integrated with distributed generators using CNN. Electr Power Syst Res. 2021;192:106914. https://doi.org/10.1016/j.epsr.2020.106914.

[41] Alhanaf AS, Balik HH, Farsadi M. Intelligent fault detection and classification schemes for smart grids based on deep neural networks. Energies. 2023;16:7680. https://doi.org/10.3390/en16227680.

[42] Altaie AS, Abderrahim M, Alkhazraji AA. Transmission line fault classification based on the combination of scaled wavelet scalograms and CNNs using a one-side sensor for data collection. Sensors. 2024;24(7):2124. https://doi.org/10.3390/s24072124.

[43] Kumar HKP, et al. High resistance fault detection in DC microgrid using Hilbert Huang transform and vector-based ensemble optimized LSTM networks. Sci Rep. 2025;15:16039. https://doi.org/10.1038/s41598-025-00977-5.

[44] Sreelekha V, Prince A. ANFIS-based fault distance locator with active power differential-based faulty line identification algorithm for shunt and series compensated transmission line using WAMS. IEEE Access. 2023;11:91500–91510. https://doi.org/10.1109/ACCESS.2023.3307466.

[45] Dommel HW. Digital computer solution of electromagnetic transients in single- and multiphase networks. IEEE Trans Power Appar Syst. 1969;PAS-88(4):388–399. https://doi.org/10.1109/TPAS.1969.292459.

[46] Breiman L. Random forests. Mach Learn. 2001;45(1):5–32. https://doi.org/10.1023/A:1010933404324.

[47] Cortes C, Vapnik V. Support-vector networks. Mach Learn. 1995;20(3):273–297. https://doi.org/10.1007/BF00994018.